Complex Phase Behavior of Polyisoprene–Polystyrene Diblock Copolymers Near the Order–Disorder Transition

Stephan Förster, Ashish K. Khandpur, Jin Zhao, and Frank S. Bates*

Department of Chemical Engineering and Materials Science, University of Minnesota, Minneapolis, Minnesota 55455

Ian W. Hamley

Department of Physics, University of Durham, Science Laboratories, South Road, Durham DH1 3LE, U.K.

Anthony J. Ryan

Materials Science Centre, UMIST, Grosvenor Street, Manchester M1 7HS, U.K.

Wim Bras

SERC Daresbury Laboratory, Daresbury, Warrington, Cheshire WA4 4AD, U.K.

Received October 29, 1993; Revised Manuscript Received July 21, 1994®

ABSTRACT: The phase behavior of polyisoprene–polystyrene (PI–PS) diblock copolymers near the order–disorder transition was investigated using dynamic mechanical measurements, transmission electron microscopy, and small-angle X-ray and neutron scattering at polyisoprene volume fractions $0.33 < f_{PI} < 0.42$. Two new ordered morphologies have been documented between hexagonally packed cylinders (HEX) and lamellae (LAM). At low temperatures a hexagonally perforated layered (HPL) microstructure occurs, that transforms into a bicontinuous cubic phase characterized by $Ia\bar{3}d$ space group symmetry near the order–disorder transition (ODT). The ordered-bicontinuous double diamind (OBDD) phase was not found at any temperature or composition studied. We demonstrate that the bicontinuous $Ia\bar{3}d$ phase exists at equilibrium over a narrow range of compositions, $0.35 \lesssim f_{PI} \lesssim 0.40$ bounded by the HEX, LAM, HPL, and disordered states, and is restricted to within about 60 °C of the ODT, suggesting the importance of finite size effects. This cubic phase also exhibits pronounced metastability, remaining intact for extended periods of time after cooling below the $Ia\bar{3}d$–HEX or $Ia\bar{3}d$–HPL phase boundary. Cooling from above the ODT to below the PS glass transition temperature leads to a vitrified form of the $Ia\bar{3}d$ state.

1. Introduction

Phase transitions involving ordered states on a mesoscopic scale occur in a wide range of fields from solid state physics to structural biology and applied materials science. Classes of materials exhibiting this behavior include thermotropic and lyotropic liquid crystals and block copolymers. Block copolymers can be viewed as showing both *lyotropic* and *thermotropic* behavior since phase transitions can be induced by changing the composition f and temperature T, respectively. The conventional representation of phase behavior is parametrized in terms of χN and f, where N is the degree of polymerization and χ is the Flory–Huggins interaction parameter, which is proportional to T^{-1}. Typically, two limiting cases in the "phase diagram" are distinguished for the ordered regime. (Here we note that since χN and f are not actually intensive variables, this is not a proper phase diagram in strict thermodynamic terms.) In the strong segregation limit (SSL), $\chi N \gg 10$, enthalpic effects dominate, leading to an interfacial composition profile that approaches a step function. On the other hand, in the weak segregation limit (WSL), $\chi N \lesssim 10$, entropic contributions become more important, leading to a broad interface with a composition profile that tends toward a sinusoidal form. This regime encompasses the various ordered phases and the disordered phase close to the order–disorder transition.[1]

Most experimental studies on block copolymers have been performed in the strong segregation limit. Polyisoprene–polystyrene (PI–PS) diblock copolymers, the most extensively studied system,[2–4] are reported to exhibit the following ordered morphologies upon increasing the volume fraction f_{PI} of polyisoprene:[5] BCC ↔ HEX ↔ OBDD ↔ LAM ↔ HEX ↔ BCC. Here BCC denotes spheres arranged on a BCC ($Im\bar{3}m$ space group) lattice, HEX is hexagonally ordered cylinders, LAM are lamellae, and OBDD is a bicontinuous double diamond structure ($Pn\bar{3}m$ space group) that was first reported for starblock copolymers.[6] The presence of BCC, HEX, and LAM and the value of the composition f_{PI} for their corresponding phase transitions are in good agreement with theoretical calculations in the SSL.[7] Because this behavior is quite well understood, we shall refer to them as "classical" phases. Thermally induced transitions between these morphologies in the SSL are not anticipated by theory and to the best of our knowledge have not been reported. Theoretical calculations have failed to explain the occurrence of the OBDD phase.[8–10]

Hasegawa et al.[5] claim to find the OBDD on only one side of the PI–PS phase diagram, indicating a certain *asymmetry* of the phase diagram with respect to the composition f_{PI}. Also, the order–order phase transitions (OOT's) are shifted somewhat off-symmetry as a function of f_{PI}. This asymmetry has been attributed to differences in monomer volumes and backbone flexibilities of both blocks leading to conformational asymmetry as characterized by the ratio $\epsilon = (v_A^{-1}b_A^2)/(v_B^{-1}b_B^2)$, where v is the segment volume and b is the associated statistical segment length.[7,11] This ratio characterizes the relative asymmetry in conformational versus volume-filling behavior of both blocks. We have found that ϵ not only is correlated to the asymmetry of the block copolymer phase diagram but also

® Abstract published in *Advance ACS Abstracts*, October 1, 1994.

0024-9297/94/2227-6922$04.50/0

plays an important role in determining the magnitude of χ in polyolefins.[12] The following convention has been adopted when plotting the diblock copolymer phase diagram as a function of χN versus f_A: the subscript A denotes the block with the larger value of $v_A^{-1}b_A^2$; i.e., $\epsilon > 1$. Using this convention, OBDD has been reported for diblock copolymers over $0.34 \leq f_{PI} \leq 0.38$, and the classic phase transition boundaries are found to be shifted to higher f_{PI}.

Phase behavior in the WSL has been studied only recently. Experiments on polyolefin block copolymers near the ODT demonstrate the existence of multiple-ordered phases[13,14] and an overall phase behavior that is richer than expected theoretically,[16–19] particularly at compositions near the LAM ↔ HEX transition. On the $f_A > 1/2$ side (within our labeling convention) two new layered morphologies have been observed; these "intermediate" phases (phases between LAM and HEX) have been identified as hexagonally modulated lamellae (HML) and hexagonally perforated layers (HPL).[14,15] Hajduk et al.[20] have also reported an ordered bicontinuous cubic phase in a $f_{PI} = 0.66$ PI–PS diblock that is characterized by $Ia\bar{3}d$ space group symmetry. This morphology is commonly encountered in lipid–water and surfactant systems[21] and was first identified by Luzzati and Spegt[22] in 1967. It can be represented by two interpenetrating networks of tubes with 3-fold connectors or by the Gyroid surface constructed by Schoen.[23] Experiments with $f_A < 1/2$ polyolefin diblock copolymers have also revealed multiple-ordered layered phases and the $Ia\bar{3}d$ bicontinuous phase in polyolefins[24] and polystyrene–poly(vinylpyridine) (PS–PVP)[25,26] diblock copolymers near the ODT. In the present study we report the phase behavior of PI–PS diblock copolymers in the WSL near the ODT where multiple-ordered phases are most likely to occur. We focus on compositions around the LAM ↔ HEX transition and $f_A < 1/2$, where the intriguing OBDD phase has been reported. Studies of the $f_A > 1/2$ side of the PI–PS phase diagram will be a topic of a forthcoming paper.[27]

This paper is organized as follows: First, details of the sample preparation, the dynamic mechanical spectroscopy, and transmission electron microscopy (TEM) and small-angle X-ray (SAXS) and neutron (SANS) scattering experiments are given. Then we present results of dynamic mechanical measurements that were used to locate phase transition temperatures, followed by a discussion of the TEM and scattering results used to identify the morphologies of the phases. Finally, we present a tentative phase diagram for PI–PS around $f_{PI} = 0.3$–0.5 together with a comparison of these results with other block copolymer systems and lyotropic liquid crystals.

2. Experimental Section

2.1. Synthesis and Sample Preparation. Polyisoprene–polystyrene (PI–PS) diblock copolymers were synthesized by living anionic polymerization using standard procedures. The polymerization reactions were carried out at 40 °C using *sec*-butyllithium as the initiator and cyclohexane as the solvent. These conditions lead to a high degree of 1,4-addition of the isoprene (75% cis-1,4-, 20% trans-1,4-, 5% 3,4-addition[28]). Since the yield was greater than 99%, the compositions could be calculated from the ratio of the added monomers. The volume fraction of polyisoprene, f_{PI}, was obtained by using the densities 1.05 and 0.90 g/cm^3 for polystyrene and polyisoprene, respectively. The compositions and molecular weights of the samples are given in Table 1. M_n has been calculated from the initiator/monomer ratio. Although this is not a direct measure of molecular weight, our experience with this class of polymers indicates that the synthesis stoichiometry provides the most quantitative measure of M_n, rather than postpolymerization characterization methods, such as osmometry and light scattering. (In fact, our precise control over M_n is directly reflected in T_{ODT} as shown below.) All samples have a narrow molecular weight distribution ($M_w/M_n \leq 1.06$) as determined by size-exclusion chromatography (SEC).

Table 1. Molecular Characteristics and Phase Transition Temperatures

sample	f_{PI}	$10^{-4}M_n$	phase transitions[a,b]
IS-42	0.42_3	3.03	$A \xrightarrow{250} Dis$
IS-41	0.40_7	3.08	$A \xrightarrow{239} Dis$
IS-39	0.39_3	3.15	$D \xrightarrow{167} B \xrightarrow{230} Dis$
IS-38	0.37_6	3.18	$D \xrightarrow{175} B \xrightarrow{234} Dis$
IS-36	0.35_9	3.38	$C \xrightarrow{182} B \xrightarrow{245} Dis$
IS-33	0.33_1	3.68	$C \xrightarrow{285} Dis$

[a] Transition temperatures are indicated in degrees centigrade above the arrows. [b] Phase assignments are as follows: A, lamellae; B, bicontinuous $Ia\bar{3}d$; C, hexagonally packed cylinders; D, hexagonally perforated layers; Dis, disordered.

Specimens were prepared for rheology, TEM, SAXS, and SANS analysis with and without 2,6-di-*tert*-butyl-4-methylphenol (BHT). This antioxidant was added to the polymers by dissolution in toluene that contained 0.2 wt % BHT, followed by precipitation in excess methanol and vacuum drying. For samples that exhibited multiple-ordered phases, duplicate rheological testing, with and without antioxidant, was performed for all the results reported in this paper. SAXS and TEM experiments were also performed with both specimen types, while SANS measurements were conducted with pristine material. None of the results were measurably sensitive to the presence or absence of BHT.

Rheology and SANS specimens were prepared in the following way. The polymer, together with a spacer, was placed between two teflon-covered glass plates and heated to 145 °C while under vacuum. At this temperature the weight of the glass plate presses the polymer into a transparent film of a thickness equal to that of the spacer (0.5–2.0 mm). The films were further annealed for 15 h at this temperature. TEM and SAXS specimens were sealed in evacuated (<10^{-5} Torr) ampoules, annealed for 5–15 h by immersion in a temperature-controlled oil bath, and then quenched into liquid nitrogen, thereby freezing the microstructure present at the elevated temperature.

2.2. Dynamic Mechanical Experiments. The dynamic elastic and loss shear moduli, G' and G'', were determined with a Rheometrics RSAII Solids Analyzer operated in the oscillatory mode over a frequency range $0.01 \leq \omega \leq 100$ rad/s using a shear sandwich fixture at a shear amplitude of 5%. Sample temperature was controlled to within 1 °C between 100 and 300 °C with a thermally regulated nitrogen gas purge. Exposure to extreme temperatures (>200 °C) was restricted to less than 2 h for each sample. SEC traces of the samples obtained before and after the initial experiments indicated some chain scission at the highest temperatures for neat specimens. The maximum broadening (observed for IS-33 upon heating to 290 °C) led to $M_w/M_n = 1.2$. In order to insure that degradation had not affected the reported phase behavior, all samples that exhibited order–order phase transitions (OOT's) (IS-36, IS-38, and IS-39) were examined rheologically with and without antioxidant. The BHT eliminated this minor amount of degradation without affecting the OOT or ODT temperatures.

2.3. Transmission Electron Microscopy. A Reichert Ultracut S microtome was used to obtain ultrathin sections (≈70 nm) for transmission electron microscopy (TEM). Microtoming was conducted at −100 °C using glass or diamond knives. Sections were picked up on 400-mesh uncoated copper grids and then stained in the vapor of a 1.5% aqueous osmium tetroxide solution; this treatment selectively stains the polyisoprene microphase. TEM was done on a JEOL 100CX electron microscope operated at 100 kV.

2.4. Small-Angle X-ray Scattering. SAXS experiments were conducted at the synchrotron facility located at Daresbury, England. The intense beam of X-rays was monochromated with Ge(111) crystals to wavelength $\lambda = 1.50 \pm 0.01$ Å and collimated using pinhole apertures. Scattered radiation was recorded on a

quadrant area detector that extends radially 0.2 m and covers an opening area of 70° with a spatial resolution of 500 μm. A more detailed description of this facility can be found elsewhere.[29]

The results presented here were obtained from polycrystalline (i.e., polydomain) specimens in a powdered form at room temperature. Because polystyrene is glassy below about 100 °C, the morphology established at elevated temperatures can be fixed by rapidly cooling to low temperatures. Scattering patterns were azimuthally averaged to the one-dimensional form of intensity (arbitrary units) versus scattering wavevector, $|\mathbf{q}| = q = 4\pi\lambda^{-1}\sin(\theta/2)$ where θ is the scattering angle. In some experiments an attenuator was used to balance the relative intensity striking the detector at high and low q values, thus helping to resolve higher order peaks without compromising the detector response.

2.5. Small-Angle Neutron Scattering. SANS measurements were performed at the Risø National Laboratory using pinhole collimation, $\lambda = 6.0$ Å wavelength neutrons ($\Delta\lambda/\lambda = 0.09$), and a 6-m sample-to-detector distance. These experiments made use of the *in situ* shearing device described in separate publications.[14,30] The specimen was held between aluminum plates, at a separation of 0.3 mm, maintained at a specified temperature (±1 °C) and prepared (i.e., oriented) using a reciprocating shear deformation. This shearing device is operated under helium, thereby avoiding oxidative degradation. Scattering data were acquired on an area detector and are reported in arbitrary units of intensity. Neutron scattering relied on the weak natural contrast between hydrogenous polystyrene and polyisoprene.

3. Experimental Results and Analysis

3.1. Dynamic Mechanical Experiments. Changes in the morphology of block copolymers are generally accompanied by pronounced changes in mechanical properties. Accordingly, dynamic mechanical measurements are a convenient tool for monitoring block copolymer phase behavior. It has been shown that the order–disorder transition (ODT)[31] and phase transitions between ordered phases (OOT)[13,14] can in favorable cases be conveniently detected by following the concomitant changes in the dynamic storage modulus, G'. In addition, the frequency dependence of G' and G'' (the loss modulus) often presents a characteristic signature for each morphology, so that preliminary information about the type of microstructure can sometimes be obtained from rheological measurements as well.

We performed measurements of G' and G'' as a function of temperature at heating rates of 1–2 °C/min. These experiments were done at frequencies where changes in the moduli at phase transitions were particularly pronounced. Except at the lowest temperatures (100–130 °C) near the glass transition temperature of polystyrene, the mechanical response of the system is sensitive to the morphology of the block copolymers. The molecular weights of each block are around or smaller than the critical molecular weights for entanglement coupling ($M_e = 5000$ for polyisoprene and 18 000 for polystyrene[32]). Except at the lowest temperatures, the frequencies employed (0.1–1 rad/s) are below the entanglement relaxation time so that at higher temperatures the microdomains dominate the mechanical response. The shear amplitude was 5% which is a compromise between having sufficient mechanical response to produce measurable stresses while remaining in the linear viscoelastic regime.

Samples IS-42, IS-41, and IS-33 (Figure 1a,b,f) show a continuously decreasing elastic modulus with increasing temperature until a sudden drop is observed at 230, 232, and 285 °C, respectively. This discontinuous decrease in the moduli signals the order–disorder transition. Frequency sweeps at higher temperatures, i.e., in the disordered phase, show the expected terminal behavior $G' \propto \omega^2$ and $G'' \propto \omega$ where ω is the deformation frequency. IS-39, IS-38, and IS-36 (Figure 1c,d,e) show a considerable

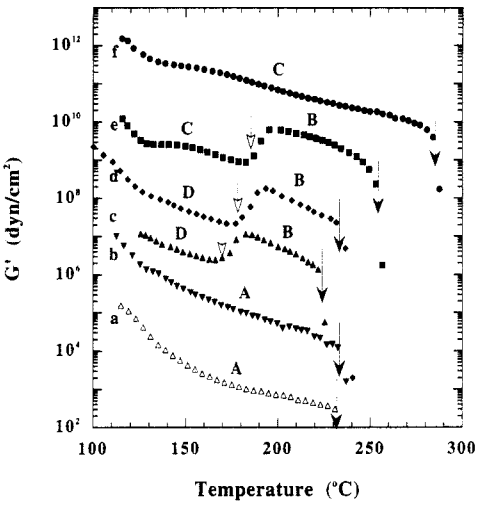

Figure 1. Dynamic storage (G') and loss (G'') moduli as a function of temperature for (a) IS-42, (b) IS-41, (c) IS-39, (d) IS-38, (e) IS-36, and (f) IS-33, at a frequency of 1 rad/s for IS-42 and 0.1 rad/s for IS-42, -39, -38, -36, and -33, and a heating rate of 2 °C/min. Phase transitions (OOT, ODT) are indicated by arrows. Phases are labeled by letters A–D. Data have been multiplied by the following factors: (a) 10°, (b) 10^3, (c) 10^3, (d) 10^4, (e) 10^6, (f) 10^8.

increase of the elastic modulus within a narrow temperature interval around 180 °C, indicating a phase transition between two ordered states. The modulus of the high-temperature phase is unusually large for a polymer melt. Upon further increase in temperature the samples eventually disorder as evident by the sudden drop in the storage modulus (224 °C for IS-39, 231 °C for IS-38, and 252 °C for IS-36). The phases and phase transition temperatures found in this study are summarized in Table 1. The ordered phase regimes are identified by the letters A–D. For the sake of simplicity, these letters are assigned to the TEM and small-angle scattering results discussed in the following sections.

Each phase exhibits a characteristic frequency dependence of the dynamic elastic and loss moduli. In Figure 2a,b isothermal frequency sweeps of phases A and C are shown, taken over a wide range of temperatures. Time–temperature superposition was attempted in order to provide a general picture of the form of these curves over a large range of frequencies for each morphology. For phase A the superposition worked quite well, while it was difficult to superimpose frequency sweeps of phase C, particularly at high temperatures. This may be due to some degree of shear-induced long-range order. It has been shown that shearing of block copolymer melts at certain temperatures and frequencies can induce long-range ordering, and the effect of orientation in the shear direction is to decrease the magnitude of the dynamic moduli.[33]

With these restrictions in mind we can nevertheless draw some qualitative conclusions concerning the mechanical response of phases A and C based on a large number of frequency sweeps with shear-oriented and unoriented samples. A exhibits the lowest dynamic moduli. The elastic and loss (not shown) moduli are continuously decreasing with increasing temperature and decreasing frequency as can be seen from a comparison of Figures 1a and 2a. $G''(\omega)$ is always larger than $G'(\omega)$, the difference being smaller than 1 order of magnitude. Phase C also shows decreasing dynamic moduli with increasing temperature and decreasing frequencies. At low frequencies and high temperatures a crossover of G' and G'' is observed. At low frequencies and high temperatures $G'(\omega) < G''(\omega)$

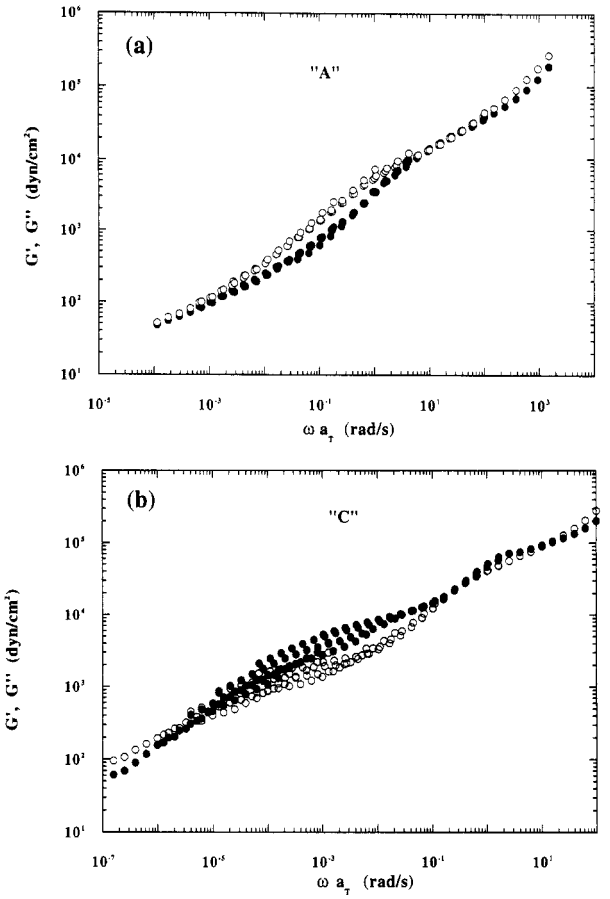

Figure 2. Dynamic storage (G', ●) and loss (G'', ○) moduli as a function of reduced frequency for (a) phase A and (b) phase C. The reference temperature is 125 °C. The shift factor follows approximately at WLF relation (not shown). Below $\omega a_T \approx 1$ rad/s the mechanical response is dominated by the topology of the microstructure.

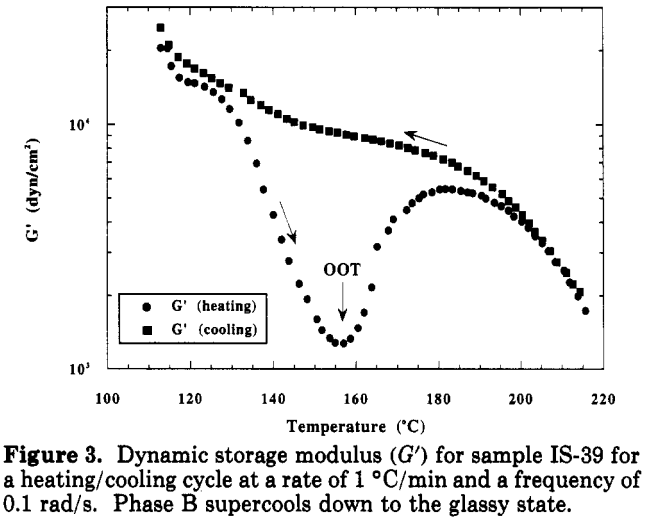

Figure 3. Dynamic storage modulus (G') for sample IS-39 for a heating/cooling cycle at a rate of 1 °C/min and a frequency of 0.1 rad/s. Phase B supercools down to the glassy state.

(see Figure 2b), the difference also being smaller than 1 order of magnitude.

A characteristic frequency dependence may therefore serve to classify certain morphologies. As an example we discuss the interesting effect of supercooling for phase B. Figure 3 shows the elastic modulus G' as a function of temperature for IS-39 at a heating rate of 1 °C/min. Upon heating the same behavior as shown in Figure 1b is observed. Starting in the glassy regime at 110 °C the modulus continuously decreases until at 165 °C the modulus starts to increase drastically, indicating the transition from D → B. After reaching 215 °C the sample was cooled at the same rate. Upon cooling the transition from B to D does not take place. Instead, the elastic modulus stays at a rather high value typical of phase B all the way into the glassy state of the polymer at 115 °C. To prove that B is still present at $T < T_{OOT}$, we performed frequency sweeps at 150 and 175 °C. Figure 4a shows phase D after heating to 150 °C. There is a distinct crossover of G' and G'' at $\omega \approx 1$ rad/s concomitant with a peak in G''. Upon heating through the phase transition the frequency dependence changes considerably. Phase B shows a high value of G' independent of frequency (Figure 4b). G'' is much smaller than G', exhibiting a minimum at $\omega \approx 3$ rad/s where the difference is nearly 2 orders of magnitude. After cooling back to 150 °C, the frequency dependence resembles that at 175 °C, except for a shift in ω due to the decreased temperature (Figure 4c). This indicates that phase B is supercooled and persists at lower temperatures. We found that the only way to recover phase D in a modest period of time ($\lesssim$2 h) was by the application of a large-amplitude shear field. Shearing the sample at a shear amplitude of 100% at 0.1 rad/s leads to the return of phase D like viscoelastic response as demonstrated by the frequency dependence shown in Figure 4d. Upon reheating the D → B transition is again observed. Thus phase B can be supercooled for intermediate periods of time (i.e., $\gtrsim$ 2 h), but phase D cannot be superheated. However, long-time annealing ($\gtrsim$10 h) at 145 °C in an evacuated (10^{-5} Torr) ampoule did produce a B → D transformation in IS-39 that was documented by TEM (see below).

We found the same supercooling behavior in samples IS-38 and IS-36. In the case of IS-36, C is the low-temperature phase. Here we note that the transition temperatures observed when heating do not depend upon the heating rate below a certain value. For example, no change in G' or G'' was observed in IS-36 after heating to, and maintaining this sample at, 150 °C for 4 h. Yet, increasing the temperature just 15 °C led to a rapid (≈5 min) transformation to phase B. These experiments indicate that D ↔ B and C ↔ B are first-order phase transitions characterized by considerable hysteresis. We will return to these observations in the Discussion section.

3.2. Transmission Electron Microscopy. Using transmission electron microscopy it was possible to identify the morphologies of phases A and C and to establish certain features of the microstructures associated with states B and D. Figure 5a shows a micrograph of phase A (IS-42 annealed at 145 °C) which can be clearly identified as having a lamellar (LAM) structure. Phase C is also easily categorized as hexagonally packed cylinders (HEX). Dark spots corresponding to the end-on view of polyisoprene cylinders along with a side view normal to the cylinder axis are seen in Figure 5b (IS-33 annealed at 145 °C).

Representative micrographs of phase B are shown in Figure 6 for IS-39; we obtained similar TEM results from each of the high-temperature phases in samples IS-36, IS-38, and IS-39, when annealed between 180 and 220 °C. These images are remarkably similar to those reported for the OBDD phase,[5,6] and we could easily misinterpret these pictures as evidence for that bicontinuous cubic microstructure. Two projections, corresponding to 3-fold (the "wagon-wheel image"[6]) and 4-fold axes of a cubic unit cell (see below), are shown. These images provide evidence for an interconnected morphology, consistent with the highly elastic character of the low-frequency viscoelastic response (Figure 4b). As discussed below we associate phase B with the bicontinuous $Ia\bar{3}d$ morphology commonly encountered in surfactant systems.[22,23]

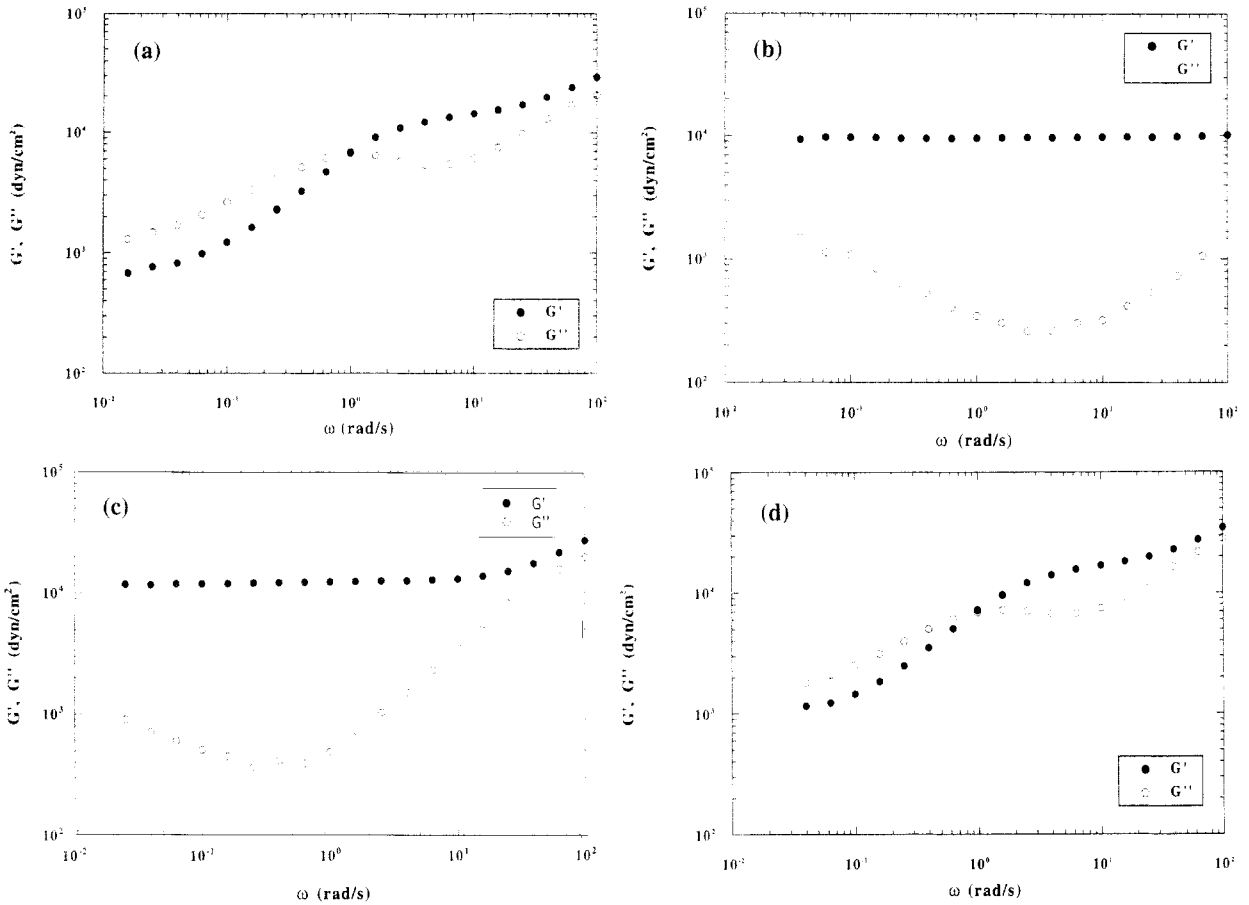

Figure 4. Dynamic storage (G') and loss (G'') moduli as a function of frequency for sample IS-39 at different stages of the heating/cooling cycle displayed in Figure 3: (a) after initially heating to 150 °C; (b) after further heating to 175 °C; (c) after subsequent cooling to 150 °C; (d) after subsequent shearing at 150 °C with a large shear amplitude. Phase B supercools, and phase D can only be recovered by application of a large-amplitude shear field.

Phase D also produced a complicated set of TEM micrographs. Two classes of images are most commonly seen in this state as shown in Figure 7 (IS-39 annealed at 145 °C). One, presented in Figure 7a, is clearly layered-like, although decidedly not lamellar. Regularly spaced perforations of the minority component are evident in this image. The second type of micrograph (inset of Figure 7) reveals white spots (PS) arranged on a dark (PI) matrix. A hexagonal symmetry can be inferred from these pictures although we cannot be certain of this point since small-angle scattering patterns have not been obtained with the beam directed along the layer normal (see below). However, this state resembles the hexagonally perforated layered (HPL) phase established in several model polyolefin and PS–PVP diblock copolymers[14,15,26] using SANS and TEM, and we tentatively associate this morphology with phase D. Here we note that HPL signifies in-plane-hexagonal perforation symmetry but *does not* imply a particular layer-by-layer stacking sequence. In fact, the stacking sequence may vary between systems that form, and do not form, the bicontinuous $Ia\bar{3}d$ phase (see below).

The rheological measurements presented in Figures 3 and 4 indicate that phase B persists in a metastable form when cooled below the order–order transition temperature (identified during heating from the low-temperature phases). TEM micrographs of the supercooled versions of IS-38 and IS-39, quenched to room temperature from 140 °C, support this picture; the images are indistinguishable from those shown in Figure 6. Upon shearing at 140 °C, or annealing at this temperature for over 10 h, images like those seen in Figure 7 were obtained, indicating a recovery of the HPL phase; these experiments confirm the equilibrium nature of these phases. However, IS-36 behaves differently, as illustrated in Figure 8. In this case, shearing at 140 °C produces two distinct microstructures, corresponding to phases B and C, despite the fact that the rheological response resembles that of phase C, which we have concluded is the equilibrium one (see below). Subsequent heating leads to the same jump in G' and G'' that is found in Figure 1e. We believe this behavior can be attributed to the drastically different rheological properties associated with each of these microstructures as described in the Discussion section.

3.3. Small-Angle X-ray Scattering. SAXS experiments were used to identify the ordered state symmetry of phase B. Three powder patterns obtained from the (quenched) high-temperature states of IS-36, IS-38, and IS-39 are presented in Figure 9. Each pattern exhibits two strong reflections at relative spacings q^* and $1.15q^*$ and a variety of less intense higher order reflections. Clearly these SAXS traces are associated with a common ordered microstructure. The subtle differences in the high-q portions of the data can be attributed to variations in the orientational distribution of the ordered grains intersected by the X-ray beam. We can identify 13 reflections in these data as listed in Table 2. The relative positions of these peaks belong to the series $\sqrt{n}q^*$ where n = 3, 4, 7, 8, 10, 11, 12, 13, 15, 16, 19, 20, 21, 23, 24, and 25 as identified by the arrows in Figure 9. This sequence of observed reflections can be indexed[22,34] as indicated in Table 2. If we assume that the first (two) observed reflection(s) correspond(s) to the first two allowed one(s),[35] then all but two space group symmetries are eliminated: $I\bar{4}3d$ and $Ia\bar{3}d$. For a variety of reasons we favor the latter.

First, there are two missing $I\bar{4}3d$ reflections, (310) and (530), within the q-range covered. However, there is also

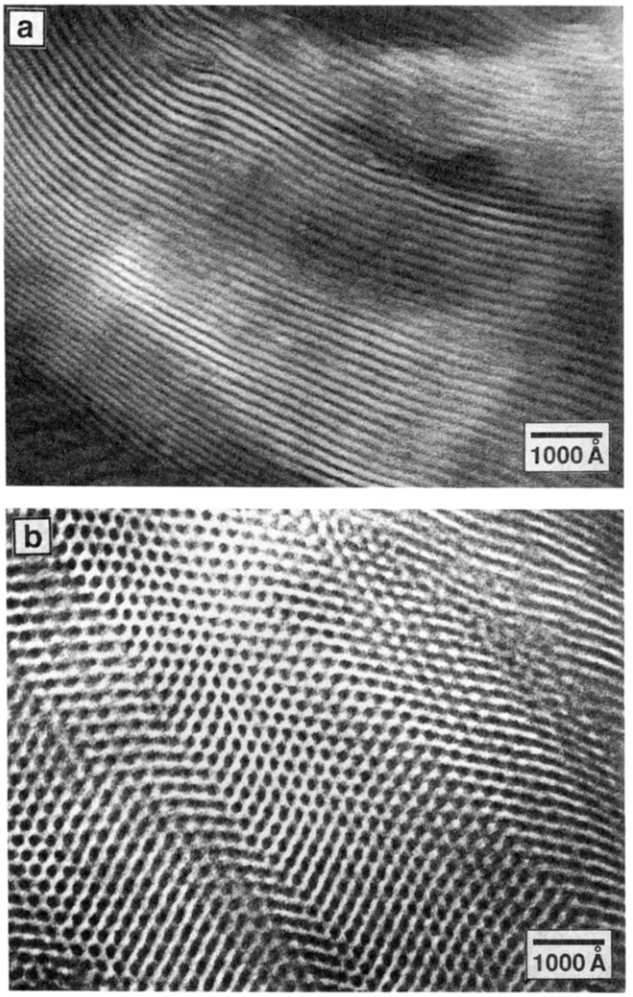

Figure 5. Transmission electron micrographs of (a) IS-42 in phase A (annealed at 145 °C) and (b) IS-33 in phase C (annealed at 145 °C), showing lamellar (LAM) and hexagonally packed cylinder (HEX) structures, respectively.

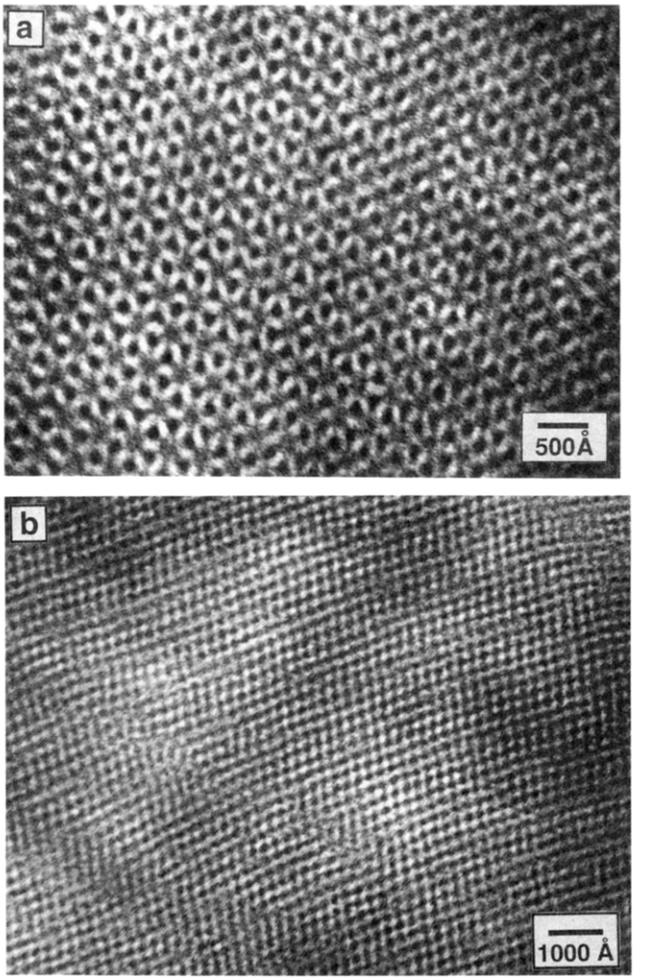

Figure 6. Representative TEM micrographs of IS-39 in phase B (annealed at 205 °C) showing (a) 3-fold and (b) 4-fold projections of the bicontinuous $Ia\bar{3}d$ microstructure.

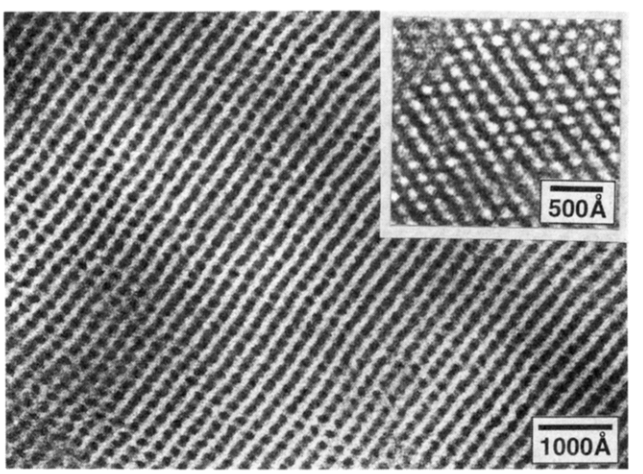

Figure 7. Representative TEM micrographs of IS-39 in phase D (annealed at 145 °C) showing projections parallel and normal (inset) to the perforated layer morphology. The hexagonal arrangement of the white (polystyrene) spots in the inset is consistent with the HPL assignment.

no evidence of the (321) reflection which should be present in either case; this may be due to a form factor extinction. Therefore, we cannot discount the $I\bar{4}3d$ symmetry on this basis alone. Second, $I\bar{4}3d$ is noncentrosymmetric.[34] Third, the 10-to-1 intensity ratio between the first and second peaks is consistent with that calculated and observed for the bicontinuous $Ia\bar{3}d$ morphology originally identified by Luzzati and Spegt.[22] Fourth, to the best of our knowledge, $I\bar{4}3d$ symmetry has never been reported for amphiphilic systems, while the bicontinuous $Ia\bar{3}d$ microstructure constitutes the most prevalent cubic phase in lipid and other surfactant systems.[21] Finally, the TEM images presented in Figure 6 are consistent with two-dimensional projections of the $Ia\bar{3}d$ bicontinuous state.[20] For these reasons we have assigned this BCC space group to phase B.

3.4. Small-Angle Neutron Scattering. SANS measurements were performed on IS-39 in order to aid in the interpretation of phase D and to further establish the low-temperature metastability of phase B. These experiments were facilitated by using the *in situ* dynamic shearing device developed in our laboratory and described in detail in separate publications.[14,15,25,30,33] A 0.3-mm-thick specimen was prepared at 145 °C (while under a helium atmosphere) using a steady reciprocating shear deformation with a strain amplitude and shear rate of $|\gamma| = 300\%$ and $\dot{\gamma} \cong 2.2\ s^{-1}$, respectively. After approximately 10 min, the shear field was stopped and the sample examined by SANS. Figure 10 depicts the deformation and neutron beam geometry for these experiments. The SANS pattern obtained roughly 30 min after cessation of shearing is presented in Figure 11a. Two well-defined reflections in the q_x–q_z scattering plane situated perpendicular to the shear direction (x) are seen; there is also evidence of off-equatorial scattering. This pattern is stable at 145 °C.

Subsequently, the specimen was heated, without shear, to 175 °C. Within 10 min a dramatic transformation

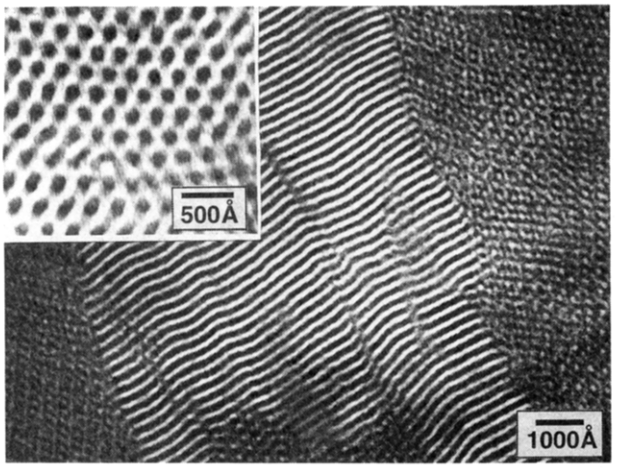

Figure 8. TEM micrographs of IS-36 obtained after cooling from 253 to 140 °C followed by shearing. Subsequently the material was annealed without shear at 140 °C for 3 h before quenching to room temperature. A mixed microstructure of HEX and bicontinuous $Ia\bar{3}d$ was obtained; the inset shows an end-on view of a cylindrical region. Coherent lattice matching at the HEX–$Ia\bar{3}d$ interfaces confirms an epitaxial relationship as shown previously.[25]

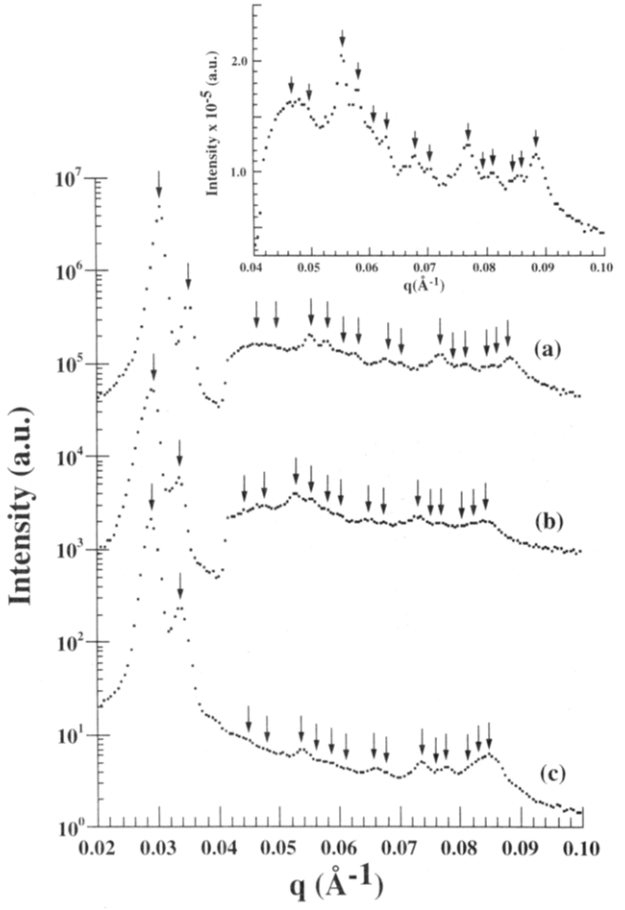

Figure 9. Small-angle X-ray scattering powder patterns obtained from the high-temperature ordered state (phase C) in (a) IS-39, (b) IS-38, and (c) IS-36. The inset is a linear version of the high-q region of a. The arrows indicate the allowed reflections for the $Ia\bar{3}d$ space group (see Table 2). These results are consistent with the bicontinuous microstructure commonly found in lyotropic liquid crystalline materials.[21] Note that the jump in intensity at 0.04 Å^{-1} in a and b results from the use of a low-q attenuator on the detector.

occurred, producing the 10-spot pattern shown in Figure 11b. This diffraction pattern persisted upon cooling to 145 °C (Figure 11c) but immediately reverted back to the

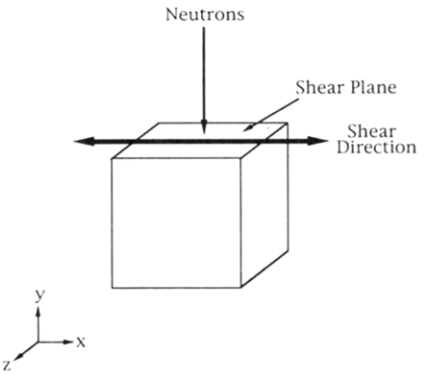

Figure 10. Coordinate system for combined dynamic shear and small-angle neutron scattering experiments.

Table 2. Allowed and Observed Reflections for the $Ia\bar{3}d$ Space Group[34]

hkl	$n^2 = h^2 + k^2 + l^2$	obsd	hkl	$n^2 = h^2 + k^2 + l^2$	obsd
211	6	×	521	30	×
220	8	×	440	32	×
321	14		611, 532	38	×
400	16	×	620	40	
420	20	×	541	42	×
332	22	×	631	46	
422	24	×	444	48	×
431	26	×	543	50	×

2-spot form when the shear deformation was applied. Upon cessation of shearing we obtained a SANS pattern (Figure 11d) very similar to that initially produced at 145 °C. In fact, now the off-equatorial reflections are better resolved. This sequence of experiments parallels the rheological experiments documented in Figure 4. We repeated this heating, cooling, and shearing cycle several times, demonstrating the metastability of phase B at temperatures below the D ↔ B order–order transition temperature (see Figure 1c). The 145 °C diffraction pattern is consistent with a layered morphology, where the layers are aligned perpendicular to the shear plane, i.e., parallel to the plane formed by the shear direction and shear gradient (see Figure 10). This orientation also occurs when (unperforated) lamellae are sheared close to the ODT as we have shown earlier.[33] These results are consistent with the hexagonally perforated layered (HPL) microstructure already associated with phase D based on TEM images (Figure 7). The 10-spot pattern obtained upon heating derives from epitaxial growth of the bicontinuous $Ia\bar{3}d$ morphology, already established by SAXS and TEM (see above). We will consider this result and the HPL phase again in the Discussion section.

4. Discussion

4.1. Phase Behavior. The results described in the previous section present a new picture of phase behavior in PI–PS diblock copolymers with $f < 1/2$. Four ordered microstructures have been identified near the order–disorder transition as illustrated in Figure 12. Two of these, hexagonally perforated layered and bicontinuous $Ia\bar{3}d$, are not classical and to the best of our knowledge have not been reported in this region of phase space. Hajduk et al.[20] have recently concluded that a $f_{PI} = 0.66$ PI–PS diblock copolymer contains the bicontinuous $Ia\bar{3}d$ morphology near T_{ODT} based on TEM and SAXS data, similar to what we have shown here.

On the basis of the transition temperatures established rheologically and assuming the temperature-dependent χ parameter reported by Rounds,[36]

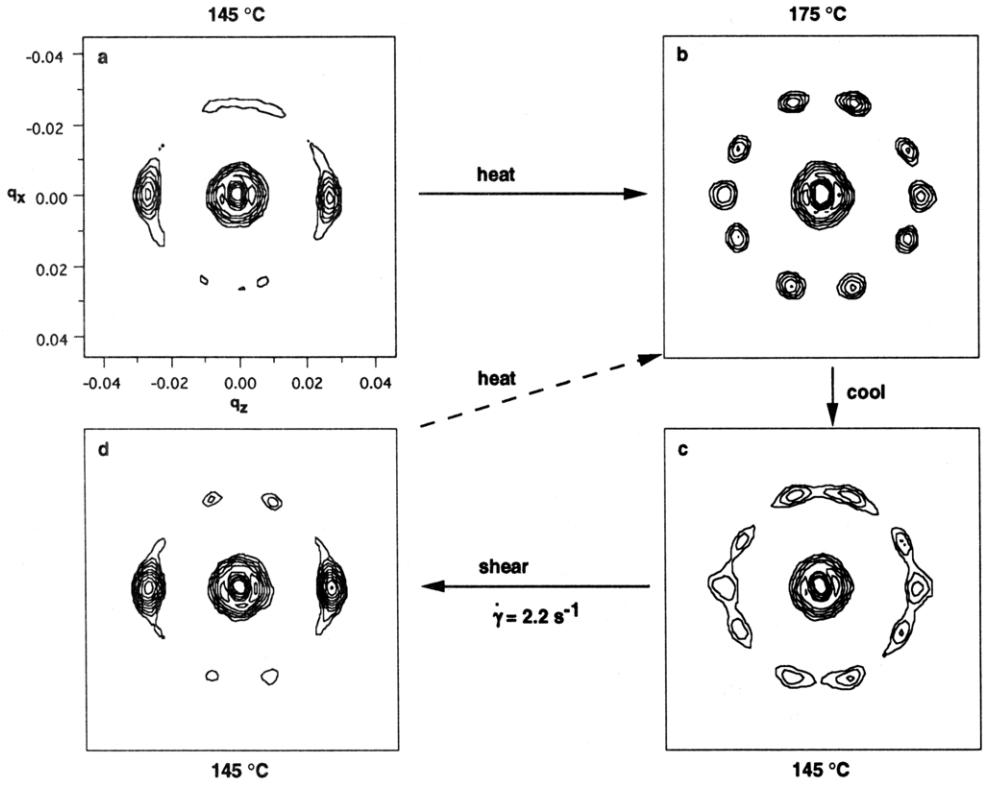

Figure 11. SANS results obtained from IS-39 demonstrating the epitaxial relationship between the HPL and bicontinuous $Ia\bar{3}d$ phases and the metastability of the later. (a) The specimen was loaded between aluminum plates and sheared at 145 °C for 10 min at $|\dot{\gamma}| = 2.25\ s^{-1}$; the shear direction is along q_x (see Figure 10). The SANS pattern was obtained after the shear deformation was stopped. (b) The 10-spot pattern, created by heating without shear, is produced by {211} reflections from the bicontinuous $Ia\bar{3}d$ phase. The angular distribution of the reflections (see text) indicates that the [111] direction is coincident with the shear direction. (c) Cooling without shear leads to a metastable bicontinuous phase. (d) Shearing rapidly converts the cubic phase back to the hexagonally perforated layer phase. The location of the off-equatorial reflection (±19.47° with respect to the shear direction) is consistent with ABC... stacking of hexagonally perforated layers. All four patterns are based on the same logarithmic intensity scale, with contour levels separated by half-decade increments.

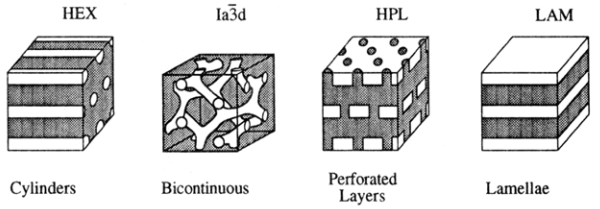

Figure 12. Illustrations of the microstructures reported in this work. These are not likely to be accurate depictions of the actual block copolymer morphologies. Near the order–disorder transition the composition profiles will become more sinusoidal-like. Also, the bicontinuous $Ia\bar{3}d$ and HPL microstructures can be constructed using a variety of interfacial models. The ones shown are topologically correct but are not intended to be interpreted quantitatively.

$$\chi = 71.4T^{-1} - 0.0857 \quad (1)$$

we have prepared the tentative phase diagram for $f_{PI} < 1/2$ illustrated in Figure 13. Here, N and χ are both based on the statistical volume $v = (v_{PI}v_{PS})^{1/2} \cong 1.44 \times 10^{-22}\ cm^3$. The points identified in Figure 13 correspond to the experimentally determined OOT and ODT χN values, while the solid curves have been sketched in a manner consistent with our phase assignments. We must emphasize that this depiction does not rule out the possibility of finding additional phases at intermediate values of f_{PI}. Crosses identify the experimental limit in χN dictated by the PS glass transition temperature.

This phase diagram should be compared with the results of a comprehensive study by Hasegawa et al.[5] on solvent-cast PI–PS diblock copolymers in the strong segregation limit (SSL). We should note, however, that their system

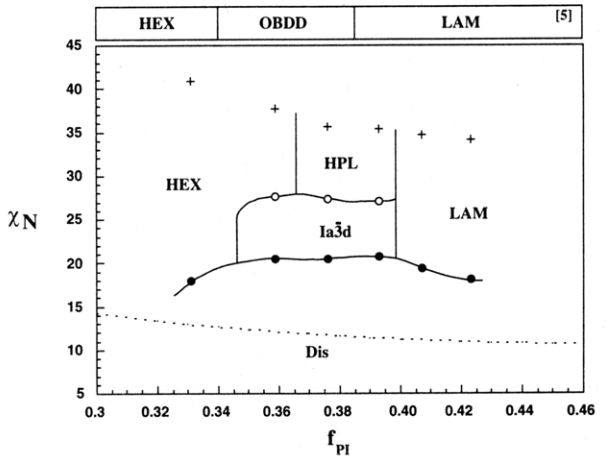

Figure 13. Phase diagram of PI–PS diblock copolymers featuring the results of the present study. The top row represents literature data[5] in the strong segregation limit. Points (●, ○) have been calculated using eq 1 and the rheologically determined transition temperatures. Crosses indicate the experimental limit set by the glass transition temperature of polystyrene. The dashed line represents the mean-field order–disorder transition.[16] Solid curves have been drawn in order to delineate the different phases but may not correspond to the precise phase boundaries.

is somewhat different from ours since the polyisoprene blocks contain a much higher fraction of vinyl (3,4 and 1,2) repeat units. Although this may not affect the overall topology (i.e., types of phases present), it could shift the location of order–order transition curves since ϵ will be different for that system. Hasegawa et al.[5] focused on the strong segregation limit, where the OOT curves can be

represented by nearly vertical lines at constant values of f_{PI}. Therefore, their results can be reduced to a one-dimensional form as shown above our phase diagram in Figure 13. These two sets of data are qualitatively different, although the windows of nonclassical phases are closely correlated in terms of f_{PI}. Hasegawa et al.[5] report the OBDD phase (a bicontinuous structure composed of tetragonal connectors with a $Pn\bar{3}m$ space group) between $f_{PI} = 0.34$ and 0.38, while we do not observe this phase at any temperature or composition. We speculate on possible reasons for the disparity between their result and ours later in the Discussion.

Although we do not attempt to rationalize the occurrence of the HPL and $Ia\bar{3}d$ phases on theoretical grounds, one topological similarity between these microstructures should be identified. Both structures can be generated from a planar tripod as illustrated in Figure 14. A hexagonally perforated layer is obtained by connecting such units in a planar fashion, i.e., with the angle of rotation between the planes associated with each tripod set to $\psi = 0$. The bicontinuous microstructure is produced by performing the symmetry operations associated with the $Ia\bar{3}d$ space group leading to $\psi = 70.53°$. (The true asymmetric unit is actually one-third of a tripod.[34] Since both structures can be formed from the same planar tripod element, it is not surprising that these phases occur adjacent to each other as the differences in chain packing must be rather small.

An even more delicate distinction can be identified in the various stacking sequences for the HPL (and the related hexagonally modulated lamellar (HML)[14,15]) phase. Two possibilities, ABAB... and ABC..., are sketched in Figure 15. Both are based on planar hexagonally perforated layers that derive from the $\psi = 0$ structure shown in Figure 14. Of course, the actual microdomains will not have sharp domain boundaries and need not conform to the tubular form depicted; these are only meant to convey the topological features. Each of these structures can be characterized by three length scales: d^* (interlayer spacing), d' (in-plane spacing), and d''. These are related through the angle γ by,

$$\tan \gamma = d'/nd^* \tag{2}$$

and

$$\cos \gamma = d''/d' \tag{3}$$

where $n = 2$ for ABAB... and $n = 3$ for ABC.... Since we always find that the equatorial and off-equatorial reflections occur at q^* with the neutron beam directed parallel to the layers (i.e., along y in Figure 15, see refs 14 and 15), we will assume $d'' = d^*$. This reduces eqs 2 and 3 to:

$$\gamma = \sin^{-1}(1/2) = 30° \quad \text{and} \quad d' = 1.15d^*$$

for ABAB... stacking and to

$$\gamma = \sin^{-1}(1/3) = 19.47°, \; d' = 1.06d^*, \; \text{and} \; d''' = 0.866d^*$$

for ABC... stacking. In both cases the in-plane spacing is slightly larger than the layer spacing, in close agreement with our previous result,[14,15] $d' \cong 1.1d^*$. $\gamma = \sin^{-1}(1/3)$ exactly corresponds to the position of the off-equatorial reflections found in Figure 11d, leading us to tentatively conclude that the HPL phase in the PI–PS specimens is composed of an ABC... stacking sequence. This may have consequences on the epitaxial growth of the bicontinuous $Ia\bar{3}d$ phase as discussed below.

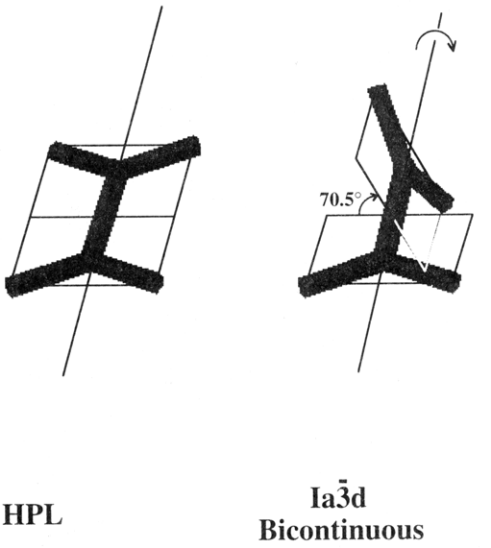

Figure 14. Simple depiction of the fundamental topology associated with the HPL and bicontinuous $Ia\bar{3}d$ microstructures. Planar connection ($\psi = 0$) of planar tripods leads to the HPL structure, while the rotation $\psi = 70.53°$ followed by the appropriate symmetry operations produces the bicontinuous morphology.

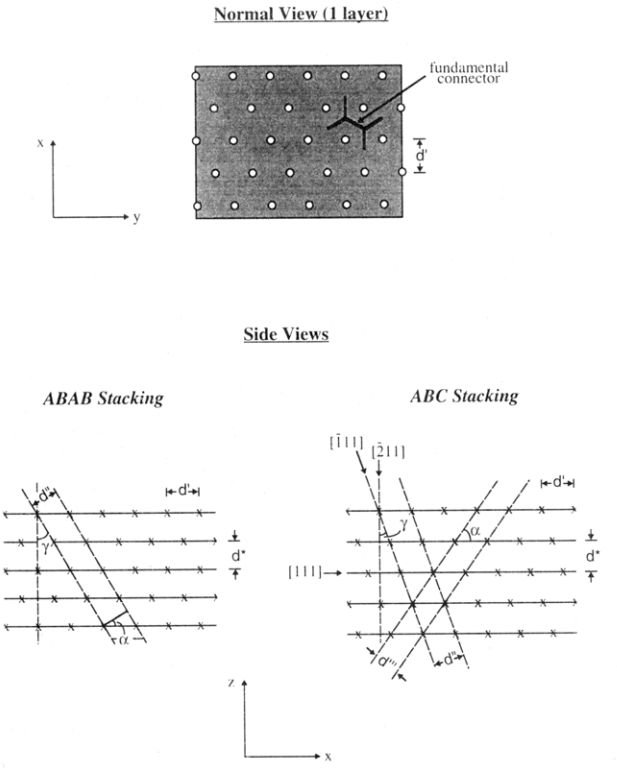

Figure 15. Stacking sequences for the HPL microstructure. A view normal to a single perforated layer is shown in the top panel. ABAB... and ABC... stacking of such layers is depicted below. Assuming $d'' = d^*$ in the ABC... system leads to the epitaxial relationship indicated by the bracketed directions, that are associated with the bicontinuous $Ia\bar{3}d$ phase.

We are not entirely satisfied with this analysis since strict ABC... stacking of hexagonally perforated sheets, where the "holes" are symmetrically formed with respect to the layer normal, would produce an additional set of reflections at $\alpha = \pm 35.26°$ and $q = 1.155q^*$ (see Figure 15) that are not observed. In all likelihood the actual microdomain structure is more complex, which could break the formal ABC... ($R\bar{3}m$ space group) symmetry. Moreover, we cannot exclude the possibility that the off-equatorial reflection in Figure 11d derives from a small

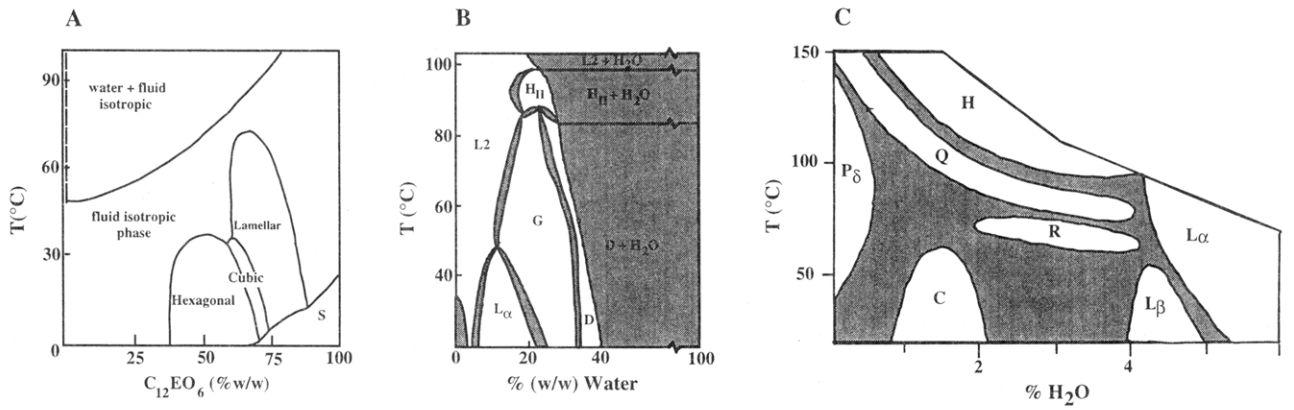

Figure 16. Representative water-based lyotropic liquid crystal phase diagrams. (A) $C_{12}EO_6$, a nonionic surfactant. The cubic phase is bicontinuous $Ia\bar{3}d$ (redrawn from ref 41). (B) Monoglyceride of oleic. G and D correspond to bicontinuous $Ia\bar{3}d$ and $Pn\bar{3}m$ (OBDD) phases, respectively. L_α, H_{II}, and L2 are lamellae, HEX cylinders, and isotropic phases, respectively (redrawn from ref 42). (C) Egg lecithin (phosphatidyl choline). L_α, L_β, and P_δ are layered phases, H is HEX cylinders, R is HPL with ABC... stacking ($R\bar{3}m$ space group), Q is bicontinuous $Ia\bar{3}d$, and C is crystalline (redrawn from ref 43).

amount of residual cubic phase (note $\psi = 90° - \gamma$, see below), although TEM analysis on sheared specimens does not support this scenario.

A complete discussion of stacking in the intermediate hexagonal layered phases lies outside the scope of this paper. However, a few additional observations will be made. There is a close analogy between this topic and the selection between HCP (ABAB...) and FCC (ABC...) in simple atomic systems, where extremely small variations in interatomic potentials dictate one symmetry over the other. We suspect that the free energies of ABAB... and ABC... stacking are also nearly degenerate in hexagonally perforated layers and are probably influenced by f, ϵ, and N. For certain combinations of these parameters they may actually be indistinguishable, and this would produce a random mixture of both, which may help explain certain puzzling aspects of our previous reports[14,15] that deal with these phases. The results reported here indicate a clear difference between the HPL phase in $f_{PI} < 1/2$ PI–PS diblock copolymers and $f > 1/2$ polyolefins;[14,15] in the latter the off-equatorial reflections occur at $30° \lesssim \gamma \lesssim 45°$.

Observation of the HPL and $Ia\bar{3}d$ phases in the PI–PS specimens should not be surprising. In an effort to understand block copolymer phase behavior near the ODT, we have been examining a variety of model materials over the past few years, and a pattern has emerged that suggests a universal behavior that depends on two parameters in addition to χN and f: conformational asymmetry, ϵ, and the magnitude of composition fluctuations which are correlated with $\bar{N} = Nb^6/v^2$.[17] As $\bar{N} \to \infty$ mean-field behavior, as described by Leibler,[16] is asymptotically approached. Decreasing $\bar{N}$ magnifies the effects of fluctuations which destroys the second-order character of the ($f = 1/2$) ODT and increases $(\chi N)_{ODT}$ over all f. This effect is manifested in the location of our ODT curve relative to the mean-field prediction as illustrated in Figure 13.

Fluctuations have been studied in considerable detail during the past 6 years, leading to the conclusion that finite molecular weight effects play an important role in the phase behavior near T_{ODT}. However, prior experiments[37–39] and theory[17,18] that deal with fluctuations have focused on the disordered state. Our collective results, which are summarized in a separate publication,[24] suggest that $\bar{N}$ is also responsible for the creation of the bicontinuous cubic state. We find that increasing $\bar{N}$ from $\bar{N}_{PI-PS} \approx 1.1 \times 10^3$ to $\bar{N}_{PE-PEP} \approx 27 \times 10^3$ (PE–PEP denotes the polyethylene–poly(ethylenepropylene) diblock copolymer system) results in extinction of the $Ia\bar{3}d$ phase. This experimental fact corroborates the idea that fluctuations are an important ingredient in the stabilization of the bicontinuous phase[24,25] which in turn is consistent with our observation that the $Ia\bar{3}d$ phase is always found to be localized near T_{ODT}, where fluctuations are predicted to be most important.[40] A complete discussion of this will form the basis of a future report. Instead of considering theoretical reasons for the observed phase behavior, we shall devote some attention to experimental results in the limit $N \to 1$, that includes lipids and other types of surfactants.

The features reported here for undiluted PI–PS diblock copolymers have also recently been reported in PI–PS/PS homopolymer mixtures at similar overall polystyrene volume fractions. Disko et al.[41] have reported a "catenoid-lamellar" structure at $\phi_{PI} = 0.33$–0.35 that appears to be topologically identical to the HPL phase. TEM micrographs, similar to those reported here, provide clear evidence of hexagonal perforations and a layered morphology. Spontak et al.[42] also find evidence for catenoid-lamellae along with the OBDD phase in PI–PS/PS mixtures at $\phi_{PI} \approx 0.34$. On the basis of the uncertainty regarding the OBDD phase assignment (see below), Spontak's results may be even closer to ours (Figure 13) than previously suspected. However, as these systems contain a considerable amount of homopolymer, the phase diagram, including composition dependence, could be qualitatively different.

There is also a striking similarity in the phase behavior and topology of normal and inverted phases in lyotropic liquid crystals and intermediate phases in PI–PS diblock copolymers. Before comparing these systems, we must identify certain differences between these related amphiphilic materials. Most surfactant-like systems are multicomponent, and the composition ϕ (e.g., water fraction) can be varied continuously. Phase diagrams are generally depicted in terms of T and ϕ, a proper thermodynamic representation. Application of the Gibbs phase rule leads to two-phase windows within which T and ϕ can both be varied. This is not possible in a one-component block copolymer melt. Nevertheless, the phase behaviors of diblock copolymers and surfactants are obviously closely related, and the latter can provide useful insights regarding the results we report here. Three representative water-based lyotropic liquid crystal phase diagrams, taken from an extensive literature (see ref 21 for a review), are shown in Figure 16: the nonionic surfactant $C_{12}EO_6$;[43] monoglyceride of oleic,[44] a simple lipid molecule; and egg lecithin,[45] a common phosphoglyceride

known as phosphatidyl choline. (Here we note that the lack of certain two-phase envelopes in the $C_{12}EO_6/H_2O$ phase diagram is inconsistent with the Gibbs phase for a two-component mixture. However, we have chosen to reproduce this illustration without alteration).

These three phase diagrams exhibit topologies very similar to that shown in Figure 13 for PI–PS. In comparing the block copolymer and lyotropic liquid crystals, we must recognize that varying the water content in the latter can produce effects similar to changing temperature. An analogous situation would be created by adding a selective solvent, or mixing PI–PS with PS or PI homopolymer. This accounts for the diagonal slant to the order–disorder phase boundaries in Figure 16. Also, since $\chi \sim T^{-1}$, the diblock copolymer phase diagram should be inverted for comparison with the lyotropics. Similar to the PI–PS system a bicontinuous cubic phase with $Ia\bar{3}d$ space group symmetry is located between lamellae (L_α phase) and hexagonally packed cylinders (H_{II} phase) and bounded by the disordered (isotropic or L_2 phase) state in parts a and b of Figure 16. Even the shapes of the order–disorder transition curves resemble that found in PI–PS, particularly in the $C_{12}EO_6$/water system, i.e., the cubic/disorder boundary is displaced to lower temperatures relative to the hexagonal and lamellar phases. An interesting feature in the monoglyceride/water system (Figure 16b) is a transformation to the $Pn\bar{3}m$ (OBDD) bicontinuous phase with increased water content. We return to this point below in considering the disparity between our results and those reported by Hasegawa et al.[5] A particularly striking comparison can be made with the lecithin/water system.[45] Both bicontinuous $Ia\bar{3}d$ (Q) and HPL (R) phases are situated between hexagonal cylinders (H) and layered phases (L_α, L_β, and P_δ). The HPL phase is actually characterized by a rhombohedral lattice ($R\bar{3}m$ space group symmetry) and corresponds to the ABC... stacking sequence described previously. The arrangement of these phases is qualitatively similar to what we report for PI–PS in Figure 13.

4.2. Metastability. A distinguishing feature of the bicontinuous $Ia\bar{3}d$ phase is its relative stability when cooled below an OOT. (Here we note that pronounced hysteresis in low molecular weight surfactant analogues is well documented.[46]) We believe this can be rationalized based on the high degree of symmetry associated with the cubic phase versus the lower symmetry of the low-temperature layered and hexagonal cylinder phases. As a consequence transformation from the cubic to the hexagonal or the layered phase will be entropically unfavorable. Moreover, due to a multitude of degenerate epitaxial growth directions (see below) the rate of nucleation can be expected to be prohibitively slow. Although the HEX → bicontinuous (assigned OBDD) transition has been reported for a relatively strongly segregated PS–PI starblock copolymer,[6] we are unaware of any evidence for the reverse transformation.

We believe this feature of bicontinuous cubic phases may play an important role in the apparent inconsistency between the phase behavior described here and that reported previously. Because they operated in the SSL, Hasagawa et al.[5] needed to prepare their samples by solvent casting. In order to minimize spurious effects that might be associated with selective solvation, they chose a relatively neutral solvent. In the event of a perfectly neutral solvent, a common assumption is that the solvent simply screens segment–segment interactions, thereby reducing χ; i.e., increasing the volume fraction of solvent ϕ_s has the same effect as increasing temperature. At a certain point during the solvent-casting process, a relatively high molecular weight block copolymer will order. Subsequent removal of residual solvent will leave an ordered microstructure that may reflect events that occurred in the solvated state. On the basis of our experience with the bicontinuous $Ia\bar{3}d$ phase, we believe that such cubic phases will be particularly stable if formed during solution casting.

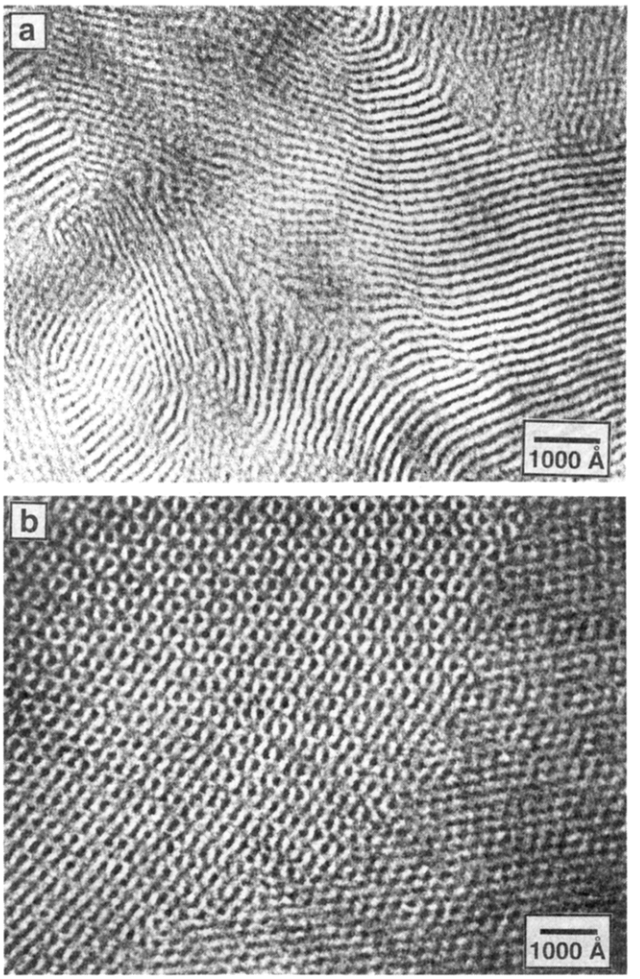

Figure 17. Representative TEM micrographs from IS-39 after (a) slow solvent casting from toluene at room temperature and (b) cooling at 1–2 °C/min from the disordered state to room temperature. Solvent casting produced the HPL phase, while cooling the melt led to a metastable bicontinuous $Ia\bar{3}d$ state.

In order to further explore this idea, we did two additional experiments. IS-39 specimens were prepared in two different ways. One was heated above T_{ODT} and slowly cooled (≈1–2 °C/min) to room temperature, while the second was solvent cast from toluene at room temperature over a period of 1 week. Assuming the simple dilution approximation $\chi = \phi_p\chi_0$ where ϕ_p is the volume fraction of polymer and χ_0 is given by eq 1, we estimate $\phi_{p,ODT} \cong 0.37$ and $\phi_{p,OOT} \cong 0.50$ based on Figure 13. These experiments produced two types of TEM images, shown in Figure 17. The one obtained by cooling closely resembles those associated with the bicontinuous $Ia\bar{3}d$ phase (Figure 6), supporting our hypothesis that a nonequilibrium cubic phase can be generated by ordering a specimen from the disordered state. However, the solvent-cast specimen adopted a perforated layered microstructure contrary to our conjecture that a bicontinuous cubic phase might form. We note, however, that the molecular weights studied by Hasegawa et al. were considerably higher than those considered here and that our solvent-casting process was quite slow.

While this metastability argument may explain how solvent casting (even in conjunction with annealing) could produce an apparent "channel" of bicontinuous cubic phase, it cannot account for the $Pn\bar{3}m$ space group and associated OBDD microstructures reported by Hasegawa et al.[5] We have no firm explanation for this inconsistency. However, the lipid/water phase diagram shown in Figure 16b may provide an important clue. In that system both the $Ia\bar{3}d$ (denoted gyroid) and $Pn\bar{3}m$ (OBDD) phases occur. Significantly, the OBDD phase does not make contact with the isotropic phase and forms the most highly solvated microstructure found in this system. This could be interpreted in two ways. First, we might deduce that the OBDD phase should appear at larger χN values (or lower temperatures) than the $Ia\bar{3}d$ window. We do not favor this interpretation due to the presence of the hexagonal and perforated layered phases above the bicontinuous cubic phase in Figure 13 and based on evidence from other systems that fail to exhibit OBDD.[24] The second hypothesis relates to the effects of solvent. Clearly, solvents do not just screen χ. Chain packing and coil dimensions will be influenced by the presence of a diluent, and we find no reason to exclude the possibility that the OBDD phase may form during solvent casting. Although far from an exact analogy, this could happen if water were evaporated at 60 °C from the simple lipid system shown in Figure 16b, provided the OBDD → $Ia\bar{3}d$ transition was kinetically constrained.

Alternatively, the bicontinuous $Ia\bar{3}d$ phase may have been inadvertently mistaken as OBDD. Simulated TEM projections of both cubic phases[20] demonstrate nearly indistinguishable images along the 3-fold and 4-fold axes, and recent SAXS experiments by Hajduk et al.[47] indicate that the original OBDD assignment in PI–PS starblock copolymers[6] is erroneous. Recent theoretical arguments advanced by Likhtman and Semenov[8] support our conclusion that the OBDD phase is at best metastable in PI–PS in the strong segregation limit.

4.3. Epitaxial Relationships. As we have shown, the transition from bicontinuous $Ia\bar{3}d$ to perforated layers or hexagonally packed cylinders is kinetically constrained. Yet upon heating from the low-temperature phases, the cubic phase grows quickly. These phase transitions, from low to high symmetry, appear to be governed by epitaxial relationships similar to those proposed for lyotropic liquid crystals.[21] In a separate report[25] we have identified such an epitaxial relationship for the hexagonal-to-$Ia\bar{3}d$ phase transition in the polystyrene–poly(vinylpyridine) system. The correspondence (10) ↔ ($1\bar{2}1$) between lattice planes controls the orientation of the cubic phase when grown from hexagonally packed cylinders where the associated lattice spacings are given by $d_{10} \cong d_{1\bar{2}1}$. (Note that the epitaxial relationship reported in ref 25 has been corrected by a 30° rotation around the [111] direction of the cubic unit cell.[48]) Direct evidence of such epitaxy is provided by the mixed microstructure shown in Figure 8. Careful examination of the boundary between the cylindrical and cubic regions reveals a coherent interface with long-range registry between the associated lattice planes within each phase. This interface must be extremely stable since annealing for several hours fails to convert the remaining cubic phase into the cylindrical morphology that is in equilibrium at low temperatures.

This degree of stability complicates the preparation of a pure cylindrical state from the cubic one by shearing. Because the hexagonal phase readily orients under shear and exhibits near-liquidlike viscoelastic properties when deformed along the cylinder axis,[39] it is difficult to homogeneously orient a bulk cubic specimen. Local orientation produces an inhomogeneous stress field due to heterogeneous two-phase structures as illustrated in Figure 18. Thus, once part of the specimen transforms to cylinders a lubricated flow condition exists that isolates regions of the cubic phase in a nearly stress-free state. However, the macroscopic viscoelastic behavior will primarily reflect the cylindrical morphology, so that upon heating the hexagonal-to-cubic transition is observed rheologically. Recently, we have found that application of larger strain amplitudes and higher shear rates can alleviate this difficulty to some extent.

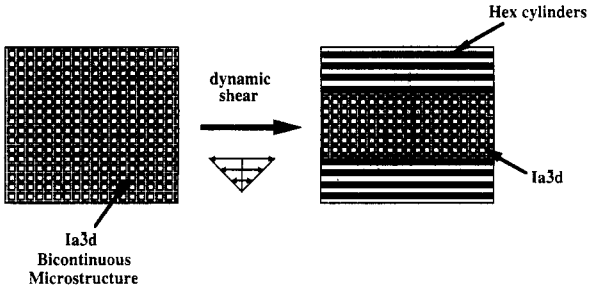

Figure 18. Illustration of the effects of dynamic shear on the metastable $Ia\bar{3}d$ state. As portions of the specimen convert to aligned hexagonally packed cylinders, a lubricated flow condition isolates the remaining cubic portion in a stress-free state.

These remarks are corroborated by the qualitatively different results we obtained for the HPL-to-$Ia\bar{3}d$ transition. In this case the low-temperature phase is not fluidlike in the oriented state, due to the presence of perforations. Presumably the more solidlike viscoelastic behavior (see Figure 4a) transmits enough stress throughout the specimen to transform essentially all the cubic material when sheared at low temperatures (see Figure 11). Similar to our findings with model polyolefins,[14,15] a well-defined, oriented (perpendicular) microstructure is obtained when the HPL phase is sheared in the neutron beam. However, the resulting scattering pattern is different from those reported elsewhere for hexagonally perforated layers (HPL) where the formation of a bicontinuous state was not observed.[14,15]

A clear epitaxial relationship exists between the low- and high-temperature phases of IS-39. Upon heating, the 2-spot pattern rapidly (5–10 min) converts into the unusual 10-spot pattern seen in Figure 11. Experience with the hexagonal-to-$Ia\bar{3}d$ epitaxy[25,43] and the reported epitaxial relationship (001) ↔ (211) between lamellae and the bicontinuous $Ia\bar{3}d$ phase in lyotropic liquid crystals[49] leads us to suspect a coincidence between the shear axis (x) and the [111] direction of the high-temperature cubic phase as identified in Figure 15. There are 24 {211} planes in a cubic lattice that can be grouped into three categories: (i) permutations with all positive or all negative indices such as (121) and ($\bar{1}\bar{1}\bar{2}$); (ii) permutations with h, k, or l being 2 or $\bar{2}$ and the remaining indices $\bar{1}$ or 1, respectively, such as ($\bar{2}11$) and ($\bar{1}2\bar{1}$); (iii) permutations with h, k, or l being 1 or $\bar{1}$ and the remaining indices $\bar{1}$ and $\bar{2}$ or 1 and 2, respectively, such as ($1\bar{2}\bar{1}$) and ($\bar{1}12$). Vectors normal to the planes in group i form an angle of ±19.47° with the [111] (and [$\bar{1}\bar{1}\bar{1}$]) direction, while groups ii and iii make angles of 90° and 61.87°, respectively. These angles correspond precisely to those found in the high-temperature SANS pattern, indicating a cubic phase with orientational order along [111]. However, all 10 reflections cannot be coplanar, indicating some degree of mosaicity and/or lack of rotational order around the [111] direction (see below).

A suggestive geometric relationship exists between the HPL (assuming ABC... stacking) and $Ia\bar{3}d$ microstructures. The angle $\gamma = \sin^{-1}(1/3)$ corresponds exactly to that produced by the group i normals (e.g., [121], see above) and the [111] direction. Also, $90° - \gamma$ is the angle formed by [111] and [$\bar{1}$11] which both lie in the (2$\bar{2}$0) plane (i.e., the shear plane). This means that the epitaxial relationship (001) ↔ ($\bar{2}$11) places the [$\bar{1}$11] direction along one set of lines connecting the centers of the "holes" in the HPL structure (see Figure 15). An epitaxial transition from a perfectly aligned (perpendicular) HPL phase to bicontinuous $Ia\bar{3}d$ would then produce six reflections in q_x–q_z situated at ±90° and ±19.47° with respect to [111] (and [$\bar{1}\bar{1}\bar{1}$]), i.e., the shear direction (x). Because there are two degenerate orientations related by a 180° rotation around [111], the ±90° reflections should be twice as intense as the other four. In practice we obtain 10 reflections, indicating less than perfect orientation around x. This could be associated with at least two effects. First, even in the best circumstances shear alignment leaves some degree of mosaic spread in the microdomain orientation. (This is actually very fortunate since perfect alignment would make the SANS measurements quite tedious.) Rocking curve experiments around the principal reflections from oriented lamellar, cylindrical, and cubic specimens[50] typically produce fwhm of 10–20°, which would account for a significant portion of the scattering at ±61.87°. Second, the phase transition is probably accompanied by some amount of local distortion that could further degrade the degree of orientational perfection. After all, block copolymer melts are rather soft materials. We find the same characteristic "10-spot" pattern when the bicontinuous $Ia\bar{3}d$ phase is grown from shear-aligned cylinders,[26,51] although increasing the degree of in-plane order can enhance the 6-spot pattern.[25] However, there is always evidence of all 10 {211} reflections that we trace to rotational misalignment and mosaicity as noted here.

Establishing the origins of the 10-spot pattern found in Figure 11 is an important result of this work. In many circumstances, it is not possible to apply the entire complement of experimental procedures used here when evaluating block copolymer systems. Due to a lack of TEM or X-ray or neutron contrast, a complete analysis may not be possible. Moreover, as $T \rightarrow T_{ODT}$ the higher-order reflections, required for powder analysis, may be lost. Simple shearing followed by small-angle scattering can provide a rather convenient (although not definitive) identification of the $Ia\bar{3}d$ phase based on what we have shown. A particularly important application is the discrimination between different cubic phases. Of the cubic space groups reported for block copolymers and lyotropic liquid crystals,[21] $Im\bar{3}m$, $Pn\bar{3}m$, and $Ia\bar{3}d$, only the latter will produce the angular relationship associated with the 10-spot pattern from first-order reflections.

5. Summary

The phase behavior of polyisoprene–polystyrene (PI–PS) diblock copolymers with $0.33 \lesssim f_{PI} \lesssim 0.42$ has been established near the order–disorder transition (ODT) using dynamic mechanical spectroscopy, transmission electron microscopy, and small-angle X-ray and neutron scattering. Four distinct phases have been identified: lamellae (LAM) hexagonally packed cylinders (HEX), a bicontinuous cubic microstructure with $Ia\bar{3}d$ space group symmetry, and a hexagonally perforated layered (HPL) morphology. There is no evidence of the ordered bicontinuous double diamond (OBDD) phase within the parameter space covered by this work. The $Ia\bar{3}d$ phase is restricted to a narrow composition window $0.35 \lesssim f_{PI} \lesssim 0.40$ near the ODT, $T_{ODT} - T_{Ia\bar{3}d} \lesssim 60$ °C. However, this phase is quite stable to cooling below the $Ia\bar{3}d$–HPL, and especially the $Ia\bar{3}d$–HEX phase boundaries, and is easily trapped by vitrification of the polystyrene block. Growth of the bicontinuous $Ia\bar{3}d$ structure from the lower symmetry HEX and HPL states is governed by epitaxial relationships that produce distinctive small-angle scattering patterns when the transformation occurs in shear-oriented material. This effect provides a useful means of identifying this new morphology.

Acknowledgment. Support for this research was provided by the U.S. Air Force Office of Scientific Research (AFOSR0-90-0207 and AF/F49620-93-1-0182) and the Center for Interfacial Engineering (CIE), a NSF Engineering Research Center at the University of Minnesota. S.F. acknowledges a postdoctoral fellowship from the Deutsche Forshungsgemeinschaft. We are grateful to Ned Thomas for providing a very helpful critique of the original manuscript that led to significant improvements that are reflected in the printed version.

References and Notes

(1) Bates, F. S.; Fredrickson, G. H. *Annu. Rev. Phys. Chem.* **1990**, *41*, 525.
(2) Aggarwal, S. L., Ed. *Block Polymers*; Plenum Press: New York, 1970.
(3) Molau, G. E., Ed. *Colloidal and Morphological Behavior of Block and Graft Copolymers*; Plenum Press: New York, 1971.
(4) Gallot, B. R. M. *Adv. Polym. Sci.* **1978**, *29*, 85.
(5) Hasegawa, H.; Tanaka, H.; Yamasaki, K.; Hashimoto, T. *Macromolecules* **1987**, *20*, 1651.
(6) Thomas, E. L.; Alward, D. B.; Kinning, D. J.; Martin, D. C.; Handlin, D. L.; Fetters, L. J. *Macromolecules* **1986**, *19*, 2197.
(7) Helfand, E. In *Developments in Block Copolymers*; Goodman, I., Ed.; Applied Science: New York, 1982; Vol. I.
(8) Likhtman, A. E.; Semenov, A. N. *Macromolecules* **1994**, *27*, 3103.
(9) Anderson, D. M.; Thomas, E. L. *Macromolecules* **1988**, *21*, 3221.
(10) Hamley, I. W.; Bates, F. S. *J. Chem. Phys.* **1994**, *100*, 6813.
(11) Vavasour, J. D.; Whitmore, M. D. *Macromolecules* **1992**, *25*, 5477.
(12) Bates, F. S.; Schulz, M. F.; Rosedale, J. H.; Almdal, K. *Macromolecules* **1992**, *25*, 5547. Bates, F. S.; Fredrickson, G. H. *Macromolecules* **1994**, *27*, 1065.
(13) Almdal, K.; Koppi, K. A.; Bates, F. S.; Mortensen, K. *Macromolecules* **1992**, *25*, 1743.
(14) Hamley, I. W.; Koppi, K. A.; Rosedale, J. H.; Bates, F. S.; Almdal, K.; Mortensen, K. *Macromolecules* **1993**, *26*, 5959.
(15) Hamley, I. W.; Gehlsen, M. D.; Khandpur, A. K.; Koppi, K. A.; Rosedale, J. H.; Schulz, M. F.; Bates, F. S.; Almdal, K.; Mortensen, K. *J. Phys. II (Fr.)*, submitted for publication.
(16) Leibler, L. *Macromolecules* **1980**, *13*, 1602.
(17) Fredrickson, G. H.; Helfand, E. *J. Chem. Phys.* **1987**, *87*, 697.
(18) Barrat, J.-L.; Fredrickson, G. H. *J. Chem. Phys.* **1991**, *95*, 1281.
(19) Matsen, M. W.; Schick, M. *Phys. Rev. Lett.* **1994**, *72*, 2660.
(20) Hajduk, D. A.; Harper, P. E.; Gruner, S. M.; Honeker, C. C.; Kim, G.; Thomas, E. L.; Fetters, L. J. *Macromolecules* **1994**, *27*, 4063.
(21) Seddon, J. M. *Biochim. Biophys. Acta* **1990**, *41*, 525.
(22) Luzzati, V.; Spegt, P. A. *Nature* **1967**, *215*, 701.
(23) Schoen, A. H. NASA Technical Report No. 05541, 1970.
(24) Bates, F. S.; Schulz, M. F.; Khandpur, A. K.; Förster, S.; Rosedale, J. H.; Almdal, K.; Mortensen, K. *Faraday Discuss. Chem. Soc.*, in press.
(25) Schulz, M. F.; Bates, F. S.; Almdal, K.; Mortensen, K. *Phys. Rev. Lett.* **1994**, *73*, 86.
(26) Schulz, M. F.; Khandpur, A. K.; Bates, F. S.; Hajduk, D. A.; Gruner, S. M., in preparation.
(27) Khandpur, A. K.; Förster, S.; Bates, F. S.; Ryan, A. J.; Bras, W.; Hamley, I. W., in preparation.
(28) Bates, F. S.; Rosedale, J. H.; Bair, H. E.; Russell, T. P. *Macromolecules* **1989**, *22*, 2557.
(29) Bras, W.; Derbyshire, G. E.; Ryan, A. J.; Mant, G. R.; Felton, A.; Lewis, R. A.; Hall, C. J.; Greaves, G. N. *Nucl. Instrum. Methods Phys. Res.* **1993**, *A326*, 587.

(30) Koppi, K. A.; Tirrell, M.; Bates, F. S.; Almdal, K.; Mortensen, K. *J. Rheol.*, in press.
(31) Rosedale, J. H.; Bates, F. S. *Macromolecules* **1990**, *23*, 2329.
(32) Ferry, J. D. *Viscoelastic Properties of Polymers*, 3rd ed.; Wiley: New York, 1980.
(33) Koppi, K. A.; Tirrell, M.; Bates, F. S.; Almdal, K.; Colby, R. H. *J. Phys. II (Fr.)*, **1992**, *2*, 1941.
(34) Hahn, T., Ed. *International Tables for Crystallography*, 2nd ed.; Kluwer: Dordrecht, The Netherlands, 1989.
(35) The sequence of observed reflections could also be generated by various other cubic space groups including $Pn\bar{3}m$ which is associated with the OBDD phase. However, this would require the complete absence of numerous reflections, including leading order ones. For example, in $Pn\bar{3}m$ the (110), (111), and (200) precede (211) as allowed reflections.[34] We are not aware of any mathematical construction that anticipates the extinction of principal reflections by microdomains characterized by dimensions smaller than the lattice parameters associated with the leading order diffraction.
(36) Rounds, N. A. Ph.D. Dissertation, University of Akron, Akron, OH, 1970.
(37) Bates, F. S.; Rosedale, J. H.; Fredrickson, G. H.; Glinka, C. J. *Phys. Rev. Lett.* **1988**, *61*, 2229.
(38) Bates, F. S.; Rosedale, J. H.; Fredrickson, G. H. *J. Chem. Phys.* **1990**, *41*, 525.
(39) Almdal, K.; Bates, F. S.; Mortensen, K. *J. Chem. Phys.* **1992**, *96*, 9122.
(40) Brazovskii, S. A.; Dzyaloshinskii, I. E.; Moratov, A. R. *Zh. Eksp. Teor. Fiz.* **1987**, *93*, 1110 (*Sov. Phys. JETP* **1987**, *66*, 625).
(41) Disko, M. M.; Liang, K. S.; Behal, S. K.; Roe, R. J.; Jeon, K. J. *Macromolecules* **1993**, *26*, 2783.
(42) Spontak, R. J.; Smith, S. D.; Ashraf, A. *Macromolecules* **1993**, *26*, 956; *Polym. Commun.* **1993**, *34*, 2233.
(43) Mitchell, D. J.; Tiddy, G.; Waring, L.; Bostock, T.; McDonald, M. P. *J. Chem. Soc., Faraday Trans.* **1983**, *79*, 975.
(44) Larsson, K. *J. Phys. Chem.* **1989**, *93*, 7304.
(45) Luzzati, V.; Gulik-Krazywicki, T.; Tardieu, A. *Nature* **1968**, *218*, 1031.
(46) Turner, D. C.; Wang, Z.-G.; Gruner, S. M.; Mannock, D. A.; McElhaney, R. N. *J. Phys. II (Fr.)*, **1992**, *2*, 2039.
(47) Hajduk, D. A.; Harper, P. E.; Gruner, S. M.; Honeker, C. C.; Thomas, E. L.; Fetters, L. J. *Macromolecules*, submitted for publication.
(48) Following our initial epitaxial assignment,[25] we discovered that the hexagonal cylinder phase in PS–PVP, and certain other diblock copolymers, can assume two different orientations depending upon shear rate, duration of shearing, thermal history, and location in phase space. Owing to differences in shearing time, the orientation of the hexagonal microstructure shown in ref 25 was rotated 30° around the cylinder axis relative to the specimen that epitaxially transformed into the cubic phase. A complete description of this result will be presented in ref 26.
(49) Clerc, M.; Levelut, A. M.; Sadoc, J. F. *J. Phys. II (Fr.)*, **1991**, *1*, 1263.
(50) Bates, F. S.; Almdal, K.; Mortensen, K., unpublished results.
(51) Zhao, J.; Majumdar, D.; Bates, F. S., in preparation.